

On the possibility of primary identification of individual cosmic ray showers

A. D. Supanitsky^{a,b,*}, G. Medina-Tanco^a, A. Etchegoyen^{b,1}

^a*Instituto de Ciencias Nucleares, UNAM, Circuito Exterior S/N, Ciudad Universitaria, México D. F. 04510, México.*

^b*Departamento de Física, Comisión Nacional de Energía Atómica, Av. Gral. Paz 1499, Buenos Aires, Argentina.*

Abstract

The transition between the Galactic and extragalactic cosmic ray components could take place either in the region of the spectrum known as the second knee or in the ankle. There are several models of the transition but it is not possible to confirm or even rule out any of them from the flux measurement alone. Therefore, the measurement of the composition as a function of primary energy will play a fundamental role for the understanding of this phenomenon.

In this work we study the possibility of primary identification in an event by event basis in the ankle region, around $E = 10^{18}$ eV. We consider as case study the enhancements of the Pierre Auger Southern Observatory, which are under construction in Malagüe, Province of Mendoza, Argentina. We use a non-parametric technique to estimate the density functions, from Monte Carlo data, corresponding to different combination of mass sensitive parameters and type of primaries. These estimates are used to obtain the classification probability of protons and iron nuclei for the different combination of parameters considered. We find that, after considering all relevant fluctuations, the maximum classification probability obtained combining surface and fluorescence detectors parameters is of order of 90%.

Key words: Cosmic Rays, Chemical Composition, Classification Technique
PACS:

* Corresponding author. Present Address: Instituto de Ciencias Nucleares, UNAM, Circuito Exterior S/N, Ciudad Universitaria, México D. F. 04510, México. E-mail: supanitsky@nucleares.unam.mx.

¹ Member of Carrera del Investigador Científico, CONICET, Argentina.

1 Introduction

The cosmic ray energy spectrum presents three main features observed by several experiments, the knee, observed at around $3 - 5 \times 10^{15}$ eV [1,2,3], the second knee, observed at 4×10^{17} eV [4,5,6,7] and the ankle. There is evidence of a fourth feature situated at the end of the spectrum, the so-called GZK suppression [8,9], which would be originated by the interaction of the ultra-high energy protons with the photons of the cosmic microwave background radiation [10,11]. For the case of heavier nuclei a similar effect is expected because of their interaction with photons from the infrared and microwave backgrounds [12].

The origin of the second knee is still unclear, it has been interpreted as the end of the efficiency of the acceleration in Galactic supernova remnant shock waves, a change in the diffusion regime in our galaxy [13,14] or even the transition between the Galactic and extragalactic components of the cosmic rays [15].

The ankle is a broader feature, it has been observed by Fly's Eye [5], Haverah Park [16], Yakutsk [6], HiRes [7] and Auger [8] in Hybrid mode at approximately the same energy, $\sim 3 \times 10^{18}$ eV. AGASA also observed the ankle but at a higher energy, $\sim 10^{19}$ eV [17]. The origin of the ankle is also unknown, it can be interpreted as the transition between the Galactic and extragalactic components [18] or the result of pair production by extragalactic protons after the interaction with photons of the cosmic microwave background radiation during propagation [15].

There are three main models of the Galactic-extragalactic transition: (i) the mixed composition model [18], in which the extragalactic sources inject a spectrum of masses of the form of the corresponding to the low energy Galactic cosmic rays and for which the transition take place in the ankle, (ii) the dip model [15], in which the ankle is originated by pair production of extragalactic protons that interact with the photons of the cosmic microwave background radiation, in this scenario the transition is given at the second knee and (iii) the ankle model, a two-component transition from Galactic iron nuclei to extragalactic protons at the ankle energy [19].

In order to rule out, or even confirm any of those models, additional information is necessary besides the energy spectrum shape and absolute intensity. Detailed measurements of the composition as a function of energy would be extremely valuable to break the present degeneracy among competing models for the Galactic-extragalactic transition [20,21]. Furthermore, this kind of information could help to determine what are the highest energy accelerators in the Galaxy and provide indicatives of the kind and level of magnetohydrodynamic turbulence present in the intergalactic medium traversed by the lowest

energy cosmic ray particles [22].

Several experiments have measured the cosmic ray composition in the region where the transition takes place. Nevertheless, large discrepancies exist between different experiments and experimental techniques [23]. One of the main reasons behind the plurality of sometimes contradicting results is that the composition is determined by comparing experimental data against numerical shower simulations. These simulations include models for the relevant hadronic interactions which are extrapolations, over several orders of magnitude in center of mass energy, of accelerator data to cosmic ray energies. No doubt, this is a source of considerable uncertainties which are confirmed, to a certain extent, by the fact that there are experimental evidences of a deficit in muon content of simulated showers with respect to real data [24].

Several multi-parametric techniques for the mass identification of individual showers have been studied and discussed in the literature. The most popular include non-parametric density estimates [25,26,27] and neural networks [25,28]. In particular, in this work we use a non-parametric density estimate technique of Gaussian kernel superposition, improved by adaptive choice of the smoothing parameters, in order to estimate the identification probability of individual nuclei, under the assumption of a binary proton and iron sample. The corresponding formalism, developed here, is general and applies to a sample of any number components. However, even if the application is formally straightforward, a wide range of theoretical and experimental uncertainties renders, at present, the extension to more than two components dubious.

As case study, the mass sensitive parameters that will be available from the enhancements of the Pierre Auger Southern Observatory are considered. Auger, in its original design is able to measure cosmic rays of energies above 3×10^{18} eV with the surface array and $\lesssim 10^{18}$ eV in hybrid mode. The enhancements AMIGA (Auger Muons and Infill for the Ground Array) [29] and HEAT (High Elevation Auger Telescopes) [30], will extend the energy range down to 10^{17} eV, encompassing the second knee and ankle region where the Galactic-extragalactic transition takes place.

AMIGA will consist of 85 pairs of Cherenkov detectors and muon counters of 30 m^2 plastic scintillators buried at ~ 2.5 m of depth. These pairs constitute the AMIGA infills, which are bounded by two hexagons of 5.9 and 23.5 km^2 corresponding to arrays of 433 m and 750 m spacing, respectively. The energies at which the AMIGA arrays attain full detection efficiency independently of the primary mass, are $\sim 10^{17}$ eV and $\sim 10^{17.6}$ eV for the 433 m and 750 m arrays respectively [31]. On the other hand, HEAT consists of three additional telescopes with elevation angle ranging from 30° to 58° and located next to the fluorescence telescope building at Coihueco. They will be used in combination with the existing 3° to 30° elevation angle telescopes at that site, as well as in

hybrid mode in conjunction with the AMIGA infills.

The paper is organized as follow: in section 2 we introduce the classification technique used for the subsequent analyses together with an analytical example of application of this technique. In section 3 we describe the full Monte Carlo simulations used in the calculation of the classification probabilities. In section 4 we present the non-parametric methods used in the calculation of the classification probabilities and the results obtained for different combination of surface and fluorescence mass sensitive parameters. In section 5 we estimate the uncertainty in the determination of the composition of a sample obtained by using the classification technique introduced earlier. Finally, the discussion and conclusions are presented in section 6.

2 Classification technique

The event by event classification consists in determining the type of nucleus that originated a given event. This is usually done comparing the experimental data with simulated data. For this purpose non-parametric techniques like Bayes classifiers are very useful tools [25,26].

From the experimental data or even from simulations, several observable parameters, chosen such that they are very sensitive to the chemical composition of the primary, can be obtained. Let \vec{x} be a d -dimensional vector composed by the mass sensitive parameters considered, $S_{cl} = \{A_1, \dots, A_L\}$ the set of classes in which the the events will be classified ($S_{cl} = \{Pr, Fe\}$ in this work) and $P(\vec{x} | A_i)$ the conditional density function for the class A_i . Therefore, the probability of A_i given \vec{x} can be obtained by using the Bayes theorem [32],

$$P(A_i | \vec{x}) = \frac{P(\vec{x} | A_i) p(A_i)}{\sum_{j=1}^L P(\vec{x} | A_j) p(A_j)}, \quad (1)$$

where $p(A_i)$ gives the prior knowledge about the relative abundances of each class. In absence of any prior knowledge the prior probability distribution is assumed to be uniform,

$$p(A_i) = \frac{1}{L} \quad \text{such that} \quad \sum_{i=1}^L p(A_i) = 1. \quad (2)$$

The classification of the event is given by the class with maximum probability,

$$A^*(\vec{x}) = \operatorname{argmax}_{A \in S_{cl}} [P(A|\vec{x})], \quad (3)$$

where $A^*(\vec{x})$ is the class assigned to the event with parameters \vec{x} .

In this work, we consider the classification into proton and iron nuclei, $S_{cl} = \{Pr, Fe\}$. Therefore, in this particular case, if $P(Pr|\vec{x}) \geq 1/2$ the event with parameters \vec{x} is classified as proton, otherwise iron.

Therefore, the distribution functions $P(\vec{x} | Pr)$ and $P(\vec{x} | Fe)$ are required to classify the experimental data into proton and iron nuclei. Estimators of these distribution functions are obtained by using a non-parametric method of superposition of Gaussian kernels using the data obtained from the detailed simulation of the showers, including the response of the detectors and taking into account the effects introduced by the reconstruction methods (see section 4).

A simplified one-dimensional analytical example is introduced in the following paragraphs in order to better understand the results obtained considering parameter spaces of more than one dimension and using non-parametric techniques to estimate the distribution functions from Monte Carlo data. This particular example presents similar features to those found in the complete and more sophisticated analysis.

Let us consider the gamma distribution,

$$f(x; \alpha, \sigma) = \frac{\alpha}{\sigma \Gamma(\alpha)} \left(\frac{\alpha x}{\sigma} \right)^{\alpha-1} \exp \left(-\frac{\alpha x}{\sigma} \right) \quad (4)$$

where α and σ are parameters. It is easy to show that the mean value and the variance of this distribution are given by $E[x] = \sigma$ and $Var[x] = \sigma^2/\alpha$, respectively.

Two classes, $S_{cl} = \{a, b\}$, are considered. The corresponding distribution functions are $P(x | a) = f(x; \alpha, \sigma_a)$ and $P(x | b) = f(x; \alpha, \sigma_b)$, where the parameter α is the same for both in order to simplify the calculations. Therefore, assuming a uniform distribution for the prior probabilities, the probability of a given x is,

$$P(a | x) = \frac{P(x | a)}{P(x | a) + P(x | b)} = \frac{f(x; \alpha, \sigma_a)}{f(x; \alpha, \sigma_a) + f(x; \alpha, \sigma_b)}. \quad (5)$$

If x is a random variable distributed according to $P(x | a)$ or $P(x | b)$,

$$p_a = \frac{f(x; \alpha, \sigma_a)}{f(x; \alpha, \sigma_a) + f(x; \alpha, \sigma_b)}, \quad (6)$$

is also a random variable. Therefore, the distribution functions of p_a for the

cases in which x is distributed according to $f(x; \alpha, \sigma_a)$ and $f(x; \alpha, \sigma_b)$ are,

$$P_s(p_a) = \begin{cases} f(x(p_a); \alpha, \sigma_s) \left| \frac{dx}{dp_a}(p_a) \right| & \text{if } p_a \in I_p \\ 0 & \text{if } p_a \notin I_p \end{cases}. \quad (7)$$

where $s = a, b$, $I_p = [1/(1 + (\sigma_a/\sigma_b)^\alpha), 1]$ if $\sigma_a > \sigma_b$ and $I_p = (0, 1/(1 + (\sigma_a/\sigma_b)^\alpha)]$ if $\sigma_a < \sigma_b$ and p_a can be obtained inverting Eq. (6),

$$x(p_a) = \frac{\sigma_b \sigma_a}{\sigma_b - \sigma_a} \ln \left[\left(\frac{\sigma_a}{\sigma_b} \right)^\alpha \left(\frac{1}{p_a} - 1 \right) \right]. \quad (8)$$

The distribution functions of p_a depend on how separated, relative to their width, are $f(x; \alpha, \sigma_a)$ and $f(x; \alpha, \sigma_b)$. A measure of this separation is given by the parameter,

$$\eta = \frac{|E[x_a] - E[x_b]|}{\sqrt{\text{Var}[x_a] + \text{Var}[x_b]}} = \sqrt{\alpha} \frac{|\sigma_a - \sigma_b|}{\sqrt{\sigma_a^2 + \sigma_b^2}}, \quad (9)$$

which is larger for distributions that are more separated (relative to their width).

Figure 1 shows $P_a(p_a)$ and $P_b(p_a)$ and the corresponding distributions $f(x; \alpha, \sigma_a)$ and $f(x; \alpha, \sigma_b)$ for three different values of η . The values of η are obtained by fixing $\sigma_a = 50$ and $\sigma_b = 33$ and changing α .

From figure 1 it is seen that as η increases, the distribution functions $P_a(p_a)$ and $P_b(p_a)$ concentrate more around $p_a = 1$ and $p_a = 0$, respectively, i.e., the classification between classes a and b get better. $P_a(p_a)$ and $P_b(p_a)$ are not symmetric, this is due to the different values of the standard deviations of $f(x; \alpha, \sigma_a)$ and $f(x; \alpha, \sigma_b)$. Moreover, for the different values of η considered $P_a(p_a)$ is more concentrated around $p_a = 1$ than $P_b(p_a)$ around $p_a = 0$, this is because $\sigma_a > \sigma_b$.

The classification probabilities for classes a and b are given by,

$$P_{cl}^a = P_a(p_a \geq 1/2) = \int_{1/2}^1 dp_a P_a(p_a), \quad (10)$$

$$P_{cl}^b = P_b(p_a \leq 1/2) = \int_0^{1/2} dp_a P_b(p_a), \quad (11)$$

and the classification probability for both classes is $P_{cl} = (P_{cl}^a + P_{cl}^b)/2$. Figure 2 shows the classification probability as a function of η for classes a , b and both together. As expected, they increase with η getting closer to one.

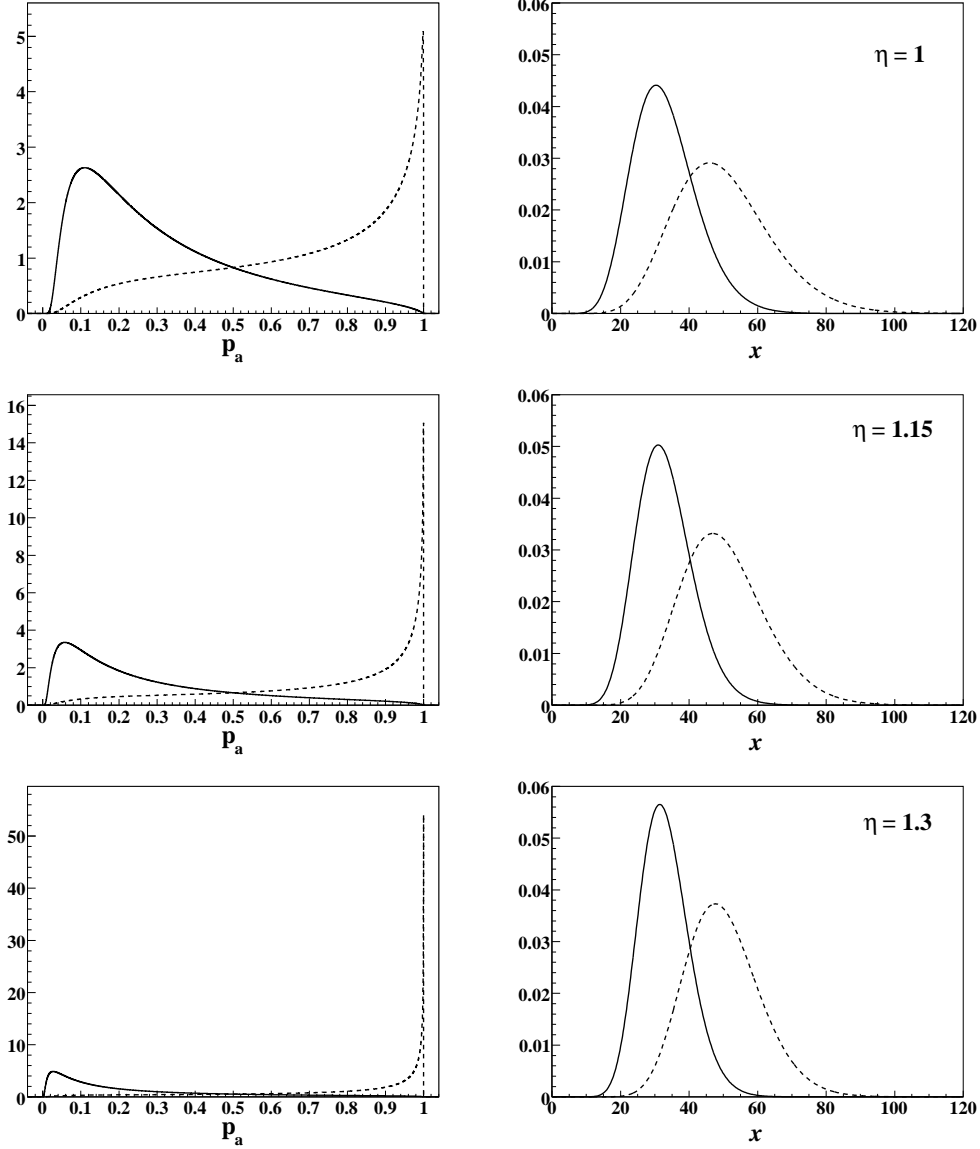


Fig. 1. Left panels show $P_a(p_a)$ and $P_b(p_a)$ as a function of p_a for three different values of η and right panels show the corresponding distributions functions $f(x; \alpha, \sigma_a)$ and $f(x; \alpha, \sigma_b)$. Dashed lines correspond to class a and solid lines to class b . The parameters $\sigma_a = 50$ and $\sigma_b = 33$ are fixed and α is varied to obtain the different values of η considered.

The classification probability, for the particular distributions considered in this example, is larger for the distribution with smaller standard deviation, this is not general, it depends on the shape of the distribution functions considered. To better understand this fact the classification probabilities can be rewritten in the following way,

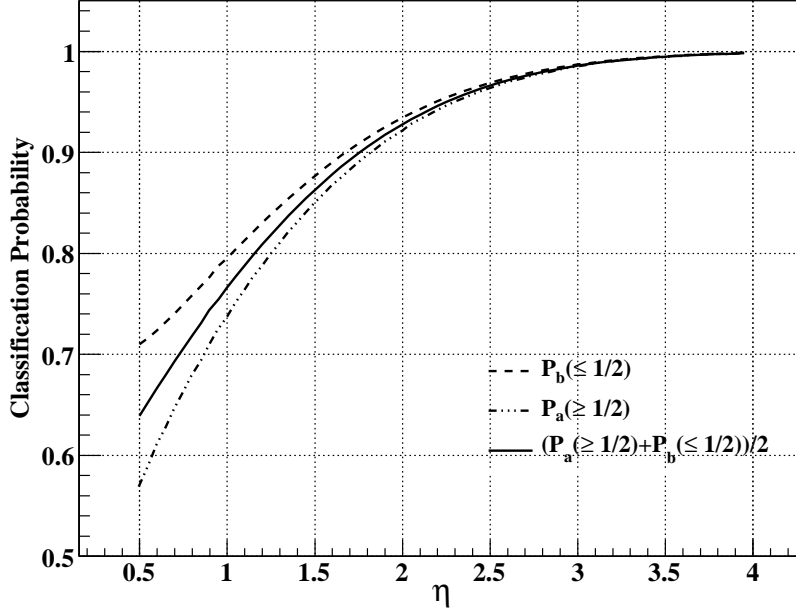


Fig. 2. Classification probability of classes a , b and a and b together as a function of η .

$$\begin{aligned}
P_{cl}^a &= \int dx \Theta(f(x; \alpha, \sigma_a) - f(x; \alpha, \sigma_b)) f(x; \alpha, \sigma_a) \\
&= \int_{x_0}^{\infty} dx f(x; \alpha, \sigma_a),
\end{aligned} \tag{12}$$

$$\begin{aligned}
P_{cl}^b &= \int dx \Theta(f(x; \alpha, \sigma_b) - f(x; \alpha, \sigma_a)) f(x; \alpha, \sigma_b) \\
&= \int_{-\infty}^{x_0} dx f(x; \alpha, \sigma_b),
\end{aligned} \tag{13}$$

where $\Theta(x) = 1$ for $x \geq 0$ and $\Theta(x) = 0$ otherwise and x_0 is the solution of $f(x_0; \alpha, \sigma_a) = f(x_0; \alpha, \sigma_b)$. The classification probability for a given class is the integral of its distribution function over the interval for which it is greater than the distribution function of the other class. Therefore, from Eqs. (12) and (13) it can be seen that although it is not general that, if the standard deviation of the distribution of class a is greater than the corresponding to class b then $P_{cl}^a < P_{cl}^b$, it happens for many different kind of distribution functions, in particular, it is true for the ones considered in this work and also for Gaussian distributions.

3 Simulations

3.1 Optimum energy bin

The primary energy estimated from the experimental data given by an array of Cherenkov detectors is obtained by fitting a lateral distribution function to the total signal in each station. This allows to interpolate the shower signal at a fixed distance from the core which, in turn, is used as an energy estimator. This reference distance is such that the shower fluctuations go through a minimum in its vicinity, and its exact value depends on the geometry of the array; for Auger, the reference distance is 1000 m for the 1500 m baseline spacing and 600 m for the AMIGA infill of 750 m of spacing.

The signal at the reference distance is calibrated with the fluorescence telescopes via hybrid events. The corresponding energy uncertainty for the 1500 m-array of Auger is $\sim 18\%$ [33]. Guided by this experimental result, we assume in this work a 25% Gaussian energy uncertainty.

The study of the classification probability at energies of order of $E_0 = 10^{18}$ eV requires the determination of the energy interval of reconstructed energies, centered at E_{r0} , defined as $\Pi_r = [(1 - \delta)E_{r0}, (1 + \delta)E_{r0}]$ ($\delta = 0.25$ for 25% of energy uncertainty) such that the fraction of events of the interval $\Pi_0 = [(1 - \delta)E_0, (1 + \delta)E_0]$ is maximum. The intervals Π_r and Π_0 are different because of the spectrum, the contamination of events of real energies smaller than 10^{18} eV which are outside Π_0 is greater than the one corresponding to energies, also outside Π_0 , but above 10^{18} eV. We follow the procedure introduced in Ref. [34] to determine Π_r which is detailed below.

The number of showers with real energies between E and $E + dE$ is given by,

$$\frac{dN}{dE}(E) = N_0 (\gamma - 1) \frac{E_1^{\gamma-1} E_2^{\gamma-1}}{E_2^{\gamma-1} - E_1^{\gamma-1}} E^{-\gamma}, \quad (14)$$

where $[E_1, E_2] = [0.1, 10] \times 10^{18}$ eV is the region of the spectrum considered, N_0 is the number of events in the interval $[E_1, E_2]$ and $\gamma = 2.7$.

The number of events whose real energies belong to Π_0 , such that the reconstructed energies fall in Π_r is,

$$f_A(E_{r0}) = \int_{(1-\delta)E_{r0}}^{(1+\delta)E_{r0}} dE \int_{(1-\delta)E_0}^{(1+\delta)E_0} dE' \frac{dN}{dE'}(E') G(E, E'), \quad (15)$$

where $G(E, E') = \exp[-(E - E')^2 / (2\delta^2 E'^2)] / (\sqrt{2\pi} \delta E')$.

On the other hand, the number of events with real energies outside Π_0 whose

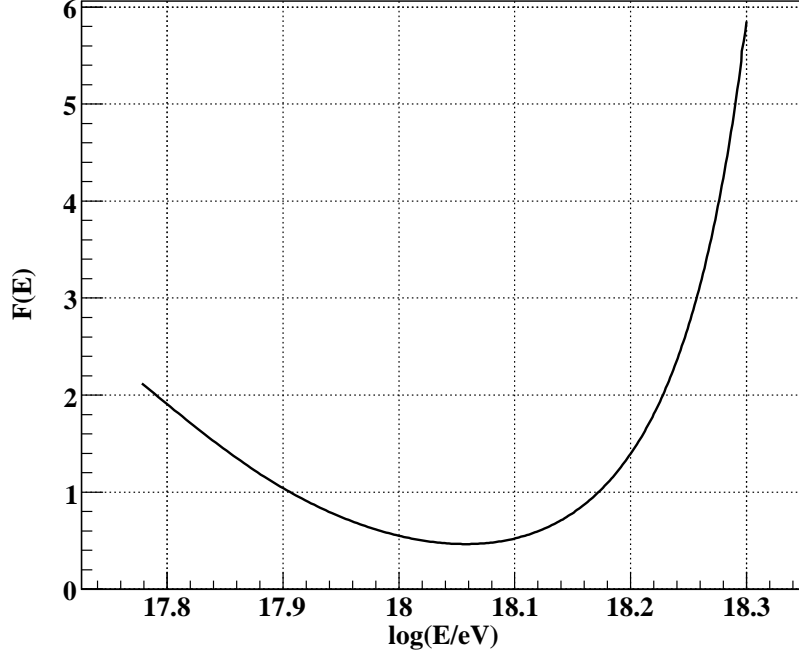


Fig. 3. Ratio between the number of events whose real energies do not belong to Π_0 but the reconstructed one fall in Π_r and the number of events whose real energies belong to Π_0 but the reconstructed one fall in Π_r , $F(E_{r0})$. The minimum is located at $E_{r0} \cong 1.14 \times 10^{18}$ eV.

reconstructed energies fall in Π_r is,

$$f_B(E_{r0}) = \int_{(1-\delta)E_{r0}}^{(1+\delta)E_{r0}} dE \left[\int_{E_1}^{(1-\delta)E_0} dE' \frac{dN}{dE'}(E') G(E, E') + \int_{(1+\delta)E_0}^{E_2} dE' \frac{dN}{dE'}(E') G(E, E') \right]. \quad (16)$$

Therefore, the value of E_{r0} for which the fraction of events belonging to Π_0 that fall in Π_r is maximum is obtained by minimizing the function $F(E_{r0}) = f_B(E_{r0})/f_A(E_{r0})$. Figure 3 shows $F(E_{r0})$ for $\delta = 0.25$ from which can be seen that it has a minimum but at an energy greater than 10^{18} eV. The minimum is located at $E_{r0} \cong 1.14 \times 10^{18}$ eV, then, $\Pi_r = [0.86, 1.43] \times 10^{18}$ eV.

The studies under consideration require the simulation of the cosmic ray energy spectrum in a large energy interval around 10^{18} eV. The number of showers required to obtain different samples of good statistics is very large. This is a very difficult task because of the computer processing time and disk space needed. The number of showers is considerably reduced considering just the events whose reconstructed energies fall in Π_r . Therefore, the distribution

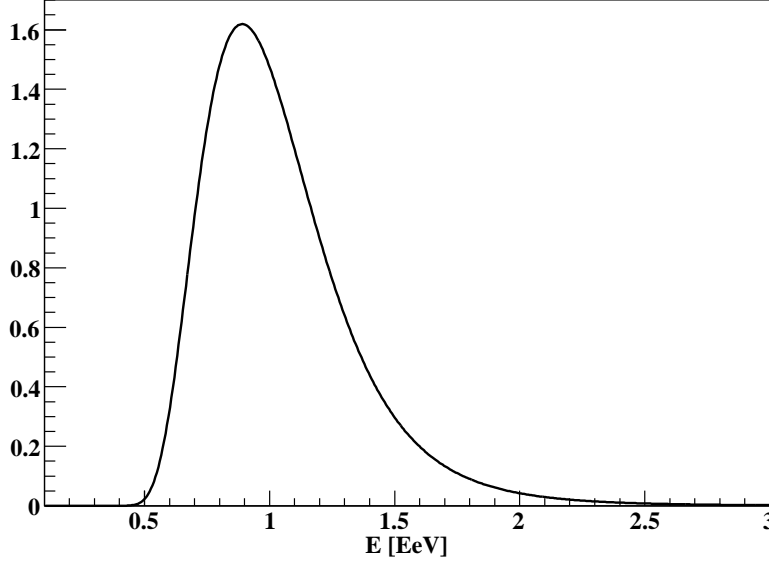


Fig. 4. Distribution function of real energies for events whose reconstructed energy falls in Π_r for $\delta = 0.25$, $\gamma = 2.7$, $E_1 = 0.1$ EeV and $E_2 = 10$ EeV.

function of real energies corresponding to events whose reconstructed energies fall in Π_r can be used to obtain the input energy for the simulations. This distribution is given by,

$$P_R(E) = C \frac{dN}{dE}(E) \int_{(1-\delta)E_{r0}}^{(1+\delta)E_{r0}} dE' G(E, E'), \quad (17)$$

where,

$$C^{-1} = \int_{E_1}^{E_2} dE \frac{dN}{dE}(E) \int_{(1-\delta)E_{r0}}^{(1+\delta)E_{r0}} dE' G(E, E'). \quad (18)$$

Performing the integral in Eq. (17) the following analytical expression is obtained,

$$P_R(E) = C E^{-\gamma} \left[\text{Erf} \left(\frac{E + E_{r0}(\delta - 1)}{\sqrt{2}\delta E} \right) - \text{Erf} \left(\frac{E - E_{r0}(\delta + 1)}{\sqrt{2}\delta E} \right) \right], \quad (19)$$

where,

$$\text{Erf}(z) = \frac{2}{\sqrt{\pi}} \int_0^z dt \exp(-t^2). \quad (20)$$

Figure 4 shows $P_R(E)$ for $\delta = 0.25$, $\gamma = 2.7$, $E_1 = 0.1 \times 10^{18}$ eV and $E_2 = 1 \times 10^{19}$ eV. The distribution of real energies is not symmetric with respect to 10^{18} eV, it has a tail at large energies due fundamentally to the assumed constant relative error on primary energy.

3.2 Showers and detector simulations

The simulation of the air showers is performed using the package Aires version 2.8.4a [35]. Firstly, 8 sets of 20 independent samples are simulated corresponding to proton and iron nuclei as primaries, zenith angles $\theta = 30^\circ$ and $\theta = 40^\circ$ and two different hadronic interaction models, QGSJET-II [36,37] and Sibyll 2.1 [38]. Each sample consists in 50 showers with primary energies obtained by taking at random 50 independent values from the distribution of Eq. (19). In this way the effects of the spectrum and energy uncertainty are taken into account (see subsection 3.1). Secondly, 8 samples of 50 showers each are also generated corresponding to proton and iron primaries, $\theta = 20^\circ, 25^\circ, 35^\circ, 45^\circ$ and QGSJET-II as the hadronic interaction model. Also in this case the input energy is obtained by sampling the distribution of Eq. (19).

The simulation of the response of the Cherenkov detectors and the muon counters of the 750 m-AMIGA array is performed by using a dedicated package described in Ref. [39]. Muon detectors of 30 m^2 of area segmented in 192 parts are used for the simulations. It is assumed a time resolution of 20 ns and the efficiency of each bar equal to one. Each shower is used 50 times by uniformly distributing impact points in the array area. The reconstruction of the arrival direction and core position of the events is performed by using the package of Ref. [40], specially developed to reconstruct the Cherenkov detector information in Auger. The muon lateral distribution function is reconstructed using the method introduced in Ref. [39] and the parameter X_{max} is obtained following the method described in Ref. [39], which takes into account the effect of the HEAT telescopes and the Reconstruction procedure of the longitudinal profile.

In short, 20 independent samples of $N \cong 50 \times 50 = 2500$ events (depending on the reconstruction efficiency) are obtained for each $\theta \in \{30^\circ, 40^\circ\}$, type of primary and hadronic interaction model. Besides, two samples of $N \cong 2500$ events are also obtained for each $\theta \in \{20^\circ, 25^\circ, 35^\circ, 45^\circ\}$ type of primary and QGSJET-II as the hadronic interaction model.

4 Numerical approach

4.1 Methodology and results

The classification method considered in this work require the knowledge of the conditional density functions $P(\vec{x} | A)$. Therefore, the non-parametric method of kernel superposition [41,42,43,44] is used to estimate the probability den-

sity functions, from the simulated data, for the different set of mass sensitive parameters considered. Besides, the adaptive bandwidth method introduced by B. Silverman [41] is also implemented in order to obtain better estimates of the density functions.

The procedure starts by performing a first estimation of each density function using a Gaussian kernel with fixed smoothing parameter,

$$\hat{P}_0(\vec{x} | A) = \frac{1}{N \sqrt{|\mathbf{V}|} (2\pi)^{d/2} h_0^d} \sum_{i=1}^N \exp \left[-\frac{(\vec{x} - \vec{x}_i)^T \mathbf{V}^{-1} (\vec{x} - \vec{x}_i)}{2h_0^2} \right], \quad (21)$$

where \vec{x} is a d -dimensional vector corresponding to one of the sets of parameters sensitive to the primary mass considered, N is the size of the sample, \mathbf{V} is the covariance matrix of the data sample and $h_0 = 1.06 \times N^{-1/(d+4)}$ is the smoothing parameter corresponding to Gaussian samples which is used very often in the literature because it gives very good estimates even for non Gaussian samples.

The following parameters are calculated by using the estimate obtained from Eq. (21),

$$\lambda_i = \left[\frac{\hat{P}_0(\vec{x}_i | A)}{\left(\prod_{j=1}^N \hat{P}_0(\vec{x}_j | A) \right)^{1/N}} \right]^{-1/2}, \quad (22)$$

and then, the final density estimate is obtained from,

$$\hat{P}(\vec{x} | A) = \frac{1}{N \sqrt{|\mathbf{V}|} (2\pi)^{d/2}} \sum_{i=1}^N \frac{1}{h_i^d} \exp \left[-\frac{(\vec{x} - \vec{x}_i)^T \mathbf{V}^{-1} (\vec{x} - \vec{x}_i)}{2h_i^2} \right], \quad (23)$$

where $h_i = h_0 \lambda_i$.

As mentioned, different type of mass sensitive parameters are used for the subsequent analyses: the depth of the maximum development of the shower, X_{max} , the number of muons at 600 m from the shower axis, $N_\mu(600)$ and a set of parameters coming from the Cherenkov detectors, $SD = \{t_{1/2}, \beta, R\}$, where $t_{1/2}$ is a parameter constructed from the individual rise-time of a subset of stations belonging to each event (see Ref. [39]), β is the slope of the lateral distribution function of the signal in the Cherenkov detectors and R is the curvature radius of the shower front. The following combination of parameters are considered: (i) $(N_\mu(600), X_{max})$, (ii) $SD = (t_{1/2}, \beta, R)$, (iii) $(N_\mu(600), SD)$, (iv) (X_{max}, SD) and (v) $All = (N_\mu(600), X_{max}, SD)$.

Ten pairs of density estimates, $\{\hat{P}_i(\vec{x} | Pr), \hat{P}_i(\vec{x} | Fe)\}$ with $i = 1 \dots 10$ are obtained for each zenith angle ($\theta = 30^\circ$ and 40°), hadronic interaction model and set of parameters. 10 of the 20 samples (see subsection 3) corresponding to protons and 10 of the 20 samples corresponding to iron nuclei are used to

construct those estimates. The rest 10 proton samples and 10 iron samples for each zenith angle and hadronic interaction model are left as test samples.

Therefore, 10 different estimates of the probability of proton given \vec{x} are obtained (see Eq. (1)),

$$\hat{P}_i(Pr|\vec{x}) = \frac{\hat{P}_i(\vec{x}|Pr)}{\hat{P}_i(\vec{x}|Pr) + \hat{P}_i(\vec{x}|Fe)} \quad \text{with } i = 1 \dots 10, \quad (24)$$

assuming no prior knowledge.

Each $\hat{P}_i(Pr|\vec{x})$ in combination with the 20 proton and iron test samples are used to obtain samples of the distributions functions, $P_{pr}(p_{pr})$ and $P_{fe}(p_{pr})$, where p_{pr} is the random variable obtained evaluating $\hat{P}_i(Pr|\vec{x})$ with a random vector \vec{x} distributed following the proton or iron distributions (see Eq. (6)). In this way, 100 samples of the distributions $P_{pr}(p_{pr})$ and $P_{fe}(p_{pr})$ are obtained for each zenith angle, hadronic interaction model and set of parameters considered.

Figure 5 shows the average, with the corresponding errors, of the 100 histograms of the samples of the distributions $P_{pr}(p_{pr})$ and $P_{fe}(p_{pr})$ corresponding to $\theta = 30^\circ$, QGSJET-II and for the different combinations of parameters considered. It shows that the best event by event classification is obtained by using all parameters because the distribution for protons is the most concentrated around one and the corresponding to iron nuclei around zero. The following best combination of parameters is $(N_\mu(600), X_{max})$ but not too far from the previous case. Although the combination (X_{max}, SD) is better than $(N_\mu(600), SD)$, the improvement in the classification probability given by the addition of $N_\mu(600)$ to the other surface detector parameters is very important because the duty cycle of the fluorescence detectors is $\sim 10\%$, which means that the size of the data sample with available X_{max} is $\sim 10\%$ of the corresponding to the surface detectors. Moreover, it is assumed, as an upper bound, 25% of energy uncertainty, presumably the energy uncertainty will be smaller, like in the higher energy range which is $\lesssim 20\%$. In this case the classification probability of the combination $(N_\mu(600), SD)$ will be equal or even better (depending on primary energy) than (X_{max}, SD) (see Ref. [39]).

Figure 5 also shows that the distribution of p_{pr} for protons are more concentrated around one than the corresponding to iron nuclei around zero. This is due to, for most of the parameters considered², the fluctuations corresponding to protons are larger, like in the simplified example of section 2.

² This is not the case for $N_\mu(600)$, for which, although the shower to shower fluctuations in the muon content are smaller for iron nuclei, when the energy uncertainty is included, they become of the same order or even larger than the ones for protons.

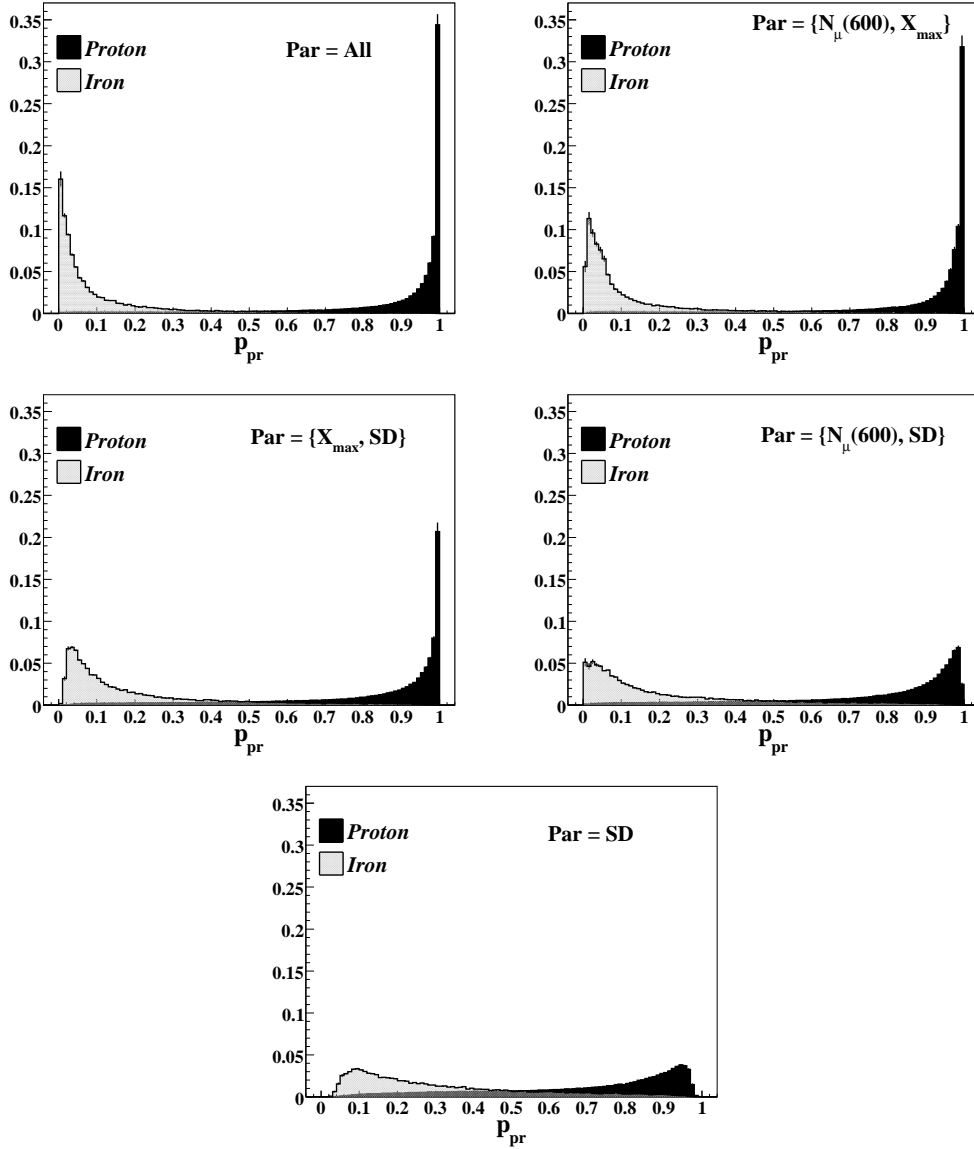


Fig. 5. Average distributions of p_{pr} with the corresponding errors for protons and iron nuclei and for the different sets of parameters considered. The zenith angle is $\theta = 30^\circ$ and the hadronic interaction model QGSJET-II.

The classification probability for protons, iron nuclei and both together are estimated from (see Eqs. (10,11)),

$$P_{cl}^{pr} = \frac{1}{N_{pr}} \sum_{i=1}^{N_{pr}} \Theta(p_{pr,i}^{pr} - 1/2) = \frac{n_{pr}}{N_{pr}}, \quad (25)$$

$$P_{cl}^{fe} = \frac{1}{N_{fe}} \sum_{i=1}^{N_{fe}} \Theta(1/2 - p_{pr,i}^{fe}) = \frac{n_{fe}}{N_{fe}}, \quad (26)$$

$$P_{cl} = \frac{N_{pr} P_{cl}^{pr} + N_{fe} P_{cl}^{fe}}{N_{pr} + N_{fe}}, \quad (27)$$

where $p_{pr,i}^A$ is the probability of i th event, corresponding to a sample of primary type $A = pr, fe$ and size N_A , to belong to the proton class and n_A is the number of events correctly classified.

Figure 6 shows the distributions of P_{cl} for QGSJET-II, $\theta = 30^\circ$ and each set of parameters considered. Consistently with the results obtained for distribution functions of p_{pr} , the highest classification probability is obtained using all parameters considered followed in decreasing order by $(N_\mu(600), X_{max})$, (X_{max}, SD) , $(N_\mu(600), SD)$ and finally SD .

Table 1 shows the medians and the regions of 68% of probability for the distributions of figure 6 and also for the corresponding to proton and iron classification probability. Although the distributions of p_{pr} for protons are more concentrated around one than the corresponding to iron around zero, the classification probabilities for iron nuclei are in general grater than for protons. This happens because, the fluctuations of the proton parameters are in general larger than for iron nuclei (see example of section 2).

Table 1

Medians and regions of 68% of probability for the classification probability distribution of protons, iron nuclei and both together, for $\theta = 30^\circ$ and hadronic interaction model QGSJET-II.

Parameters	P_{cl}^{pr}	P_{cl}^{fe}	P_{cl}
<i>All</i>	$0.91^{+0.02}_{-0.03}$	$0.92^{+0.03}_{-0.01}$	$0.92^{+0.01}_{-0.02}$
$N_\mu + X_{max}$	$0.90^{+0.03}_{-0.04}$	$0.90^{+0.04}_{-0.01}$	0.91 ± 0.02
$X_{max} + SD$	$0.86^{+0.04}_{-0.03}$	0.89 ± 0.02	0.88 ± 0.02
$N_\mu + SD$	$0.84^{+0.03}_{-0.07}$	$0.86^{+0.02}_{-0.03}$	$0.85^{+0.03}_{-0.03}$
<i>SD</i>	0.77 ± 0.03	$0.80^{+0.01}_{-0.03}$	0.78 ± 0.01

Figure 7 shows the medians and the region of 68% of probability for the classification probability distributions corresponding to the different combinations of parameters, $\theta = 30^\circ$ and $\theta = 40^\circ$ and for the hadronic interaction models QGSJET-II and Sibyll 2.1. Although the differences between the distributions corresponding to QGSJET-II and Sibyll 2.1 are small, the medians corresponding to $\theta = 40^\circ$ and QGSJET-II are systematically larger than the

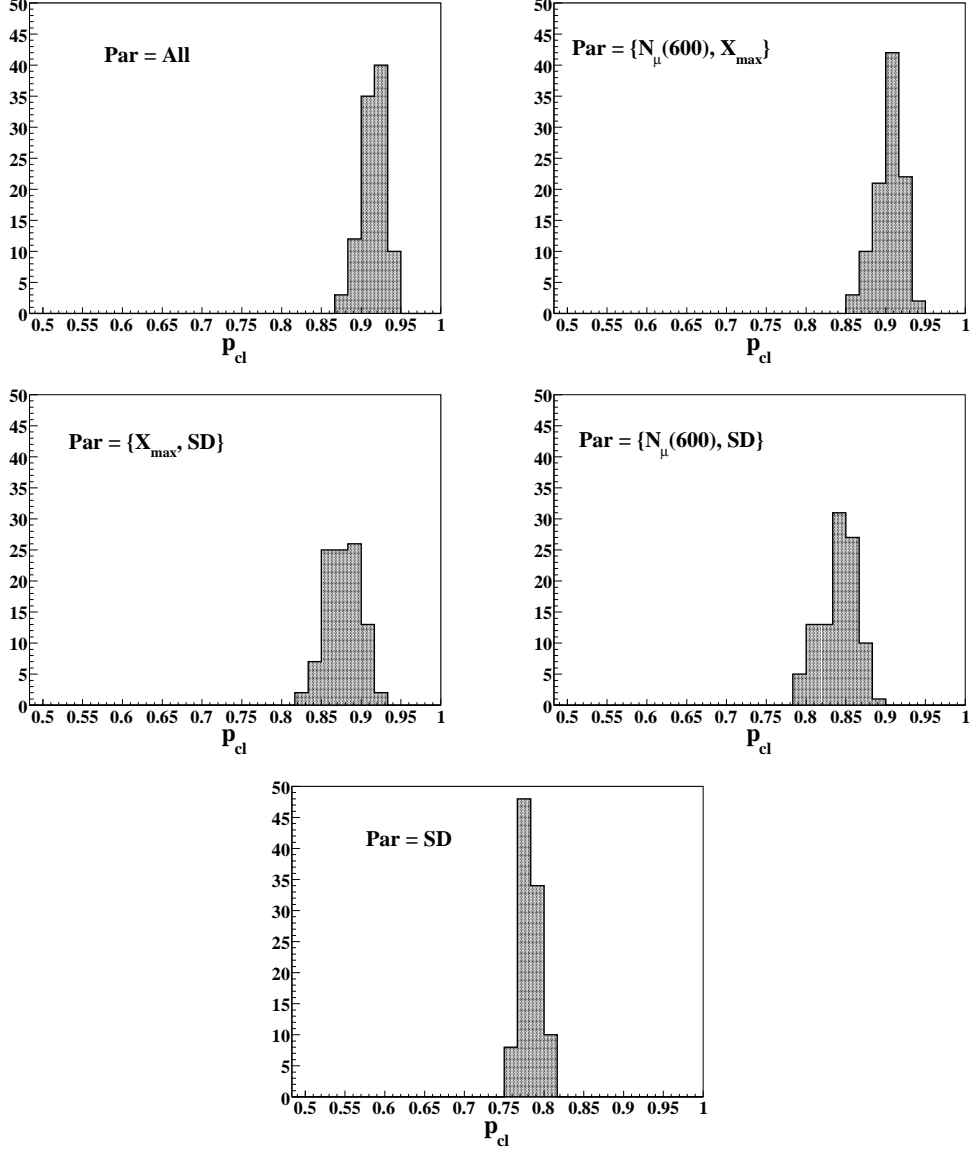


Fig. 6. Distributions of P_{cl} for $\theta = 30^\circ$ and QGSJET-II as the hadronic interaction model for the different sets of parameters considered.

corresponding to Sibyll 2.1. Besides, the classification probabilities are in general larger for $\theta = 30^\circ$, this is due to the fluctuation of the parameters are larger for $\theta = 40^\circ$.

The effect of assuming a given hadronic interaction model as the true one whereas the real one is the other is also studied. For that purpose, 20 pairs $\{\hat{P}_i(\vec{x} | Pr), \hat{P}_i(\vec{x} | Fe)\}$ with $i = 1 \dots 20$ are constructed with the proton and iron samples corresponding to QGSJET-II for $\theta = 30^\circ$ and $\theta = 40^\circ$. Then, the corresponding 20 proton samples and 20 iron samples, but generated with Sibyll 2.1, are used as test samples. In this way, the relevant distributions are obtained but assuming that QGSJET-II is the true hadronic interaction model

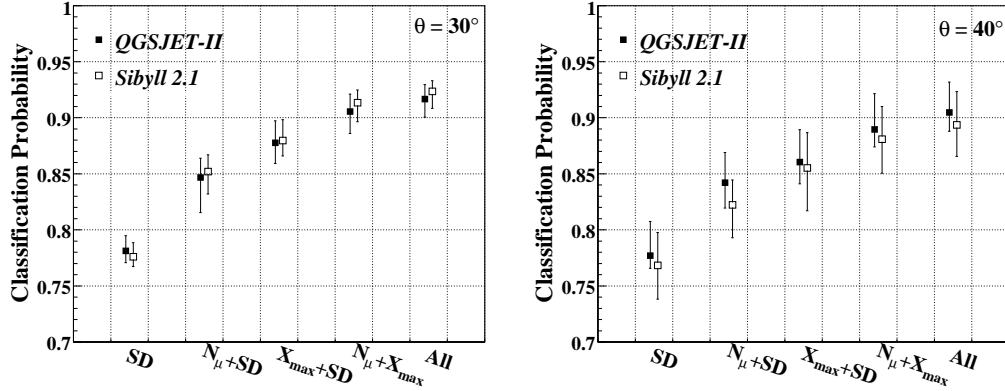


Fig. 7. Classification probability (medians and regions of 68% of probability) for the different sets of parameters considered, for $\theta = 30^\circ$ and $\theta = 40^\circ$ and for the hardronic interaction models QGSJET-II and Sibyll 2.1.

whereas the real one is Sibyll 2.1 (case $Q - S$). The same strategy is repeated but in this case assuming that Sibyll 2.1 is the true hadronic interaction model whereas the real one is QGSJET-II (case $S - Q$), i.e., the density estimates are obtained using Sibyll 2.1 samples and QGSJET-II samples are used as test samples.

Figure 8 shows the medians and the regions of 68% of probability of the classification probability distributions for the different sets of parameters considered, $\theta = 30^\circ$ and $\theta = 40^\circ$ and for both cases, $Q - S$ and $S - Q$. The classification probabilities, for the different combinations of parameters considered and for both zenith angles, result compatibles between $Q - S$ and $S - Q$ cases. This happens because the hadronic interaction models considered produce observable parameters that are quite similar between themselves. Besides, the values of the classification probabilities for the cases, $Q - S$ and $S - Q$, are compatibles with the ones obtained considering each one of those hadronic interaction models used to obtain both, the density estimates and test samples.

Note that, the previous analyses are done by using samples of events which are not independent because each shower is used 50 times to simulate the response of the detectors (see, however, Ref. [45]). This fact does not affect the present calculation, see appendix A for details.

We center here in the Auger enhancements. Consequently, we particularize our analysis for the specific properties of these detectors. Regarding detector resolution, we assume an energy error of 25%, which is much larger than the one obtained at present by the current Auger calibration with hybrid events ($\sim 18\%$). In the same way, the error in X_{max} , ΔX_{max} , is consistent with those obtained by the Auger fluorescence detectors ($\sim 20 \text{ g cm}^{-2}$ at $\sim 1 \text{ EeV}$). The resolution on the determination of $N_\mu(600)$ ($< 12\%$ for $E \geq 1 \text{ EeV}$) has been calculated in Ref. [39] specifically for the muon counters

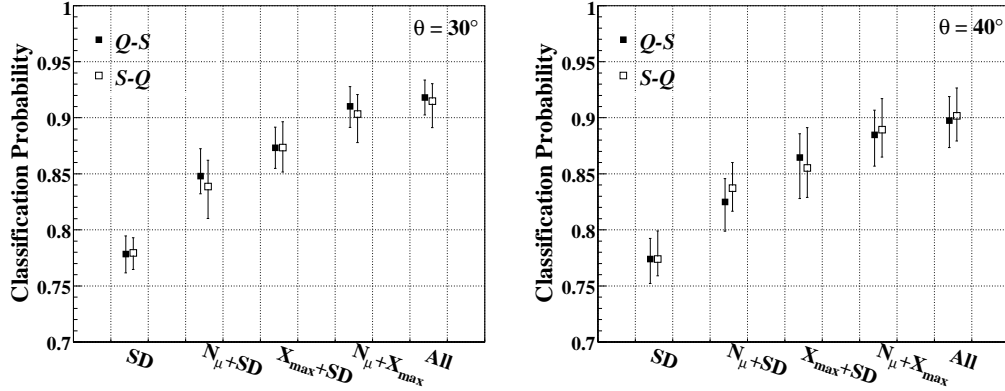


Fig. 8. Classification probability (medians and regions of 68% of probability) for the different sets of parameters considered, $\theta = 30^\circ$ and $\theta = 40^\circ$ assuming that QGSJET-II is the true hadronic interaction model whereas the real one is Sibyll 2.1 ($Q - S$) and vice versa ($S - Q$).

under consideration. Experimental uncertainties related with the simulation of the Cherenkov detectors or the reconstructed position of the core have been discussed extensively in Ref. [46] and [31], respectively, and their results have been incorporated in the calculation of the discrimination probabilities presented here.

Nevertheless, the muon counters are the only component of the system that has not been built yet beyond the prototype stage and, therefore, might be thought of as more uncertain. It can be shown that, by adding Gaussian fluctuations of magnitude α , from an unspecified origin and applied to each muon counter, the relative error in the determination of $N_\mu(600)$ increases less than 5% for $\alpha \lesssim 25\%$, which would increase the relative error from 12% to 17%. At this level, the error in energy, already included in our model, would still be dominant, leaving our conclusions unchanged.

4.2 Zenith angle dependence

The distribution functions of the different combinations of mass sensitive parameters depend on zenith angle. Therefore, as shown in figure 7, the classification probability also depends on it.

The parameter X_{max} weakly depends on θ but $N_\mu(600)$ do not. The simulations show that a new parameter, based on $N_\mu(600)$, but weakly dependent on zenith angle is obtained from,

$$\tilde{N}_\mu(600) = N_\mu(600) \left[\frac{\cos \theta_{ref}}{\cos \theta} \right]^{3/2}. \quad (28)$$

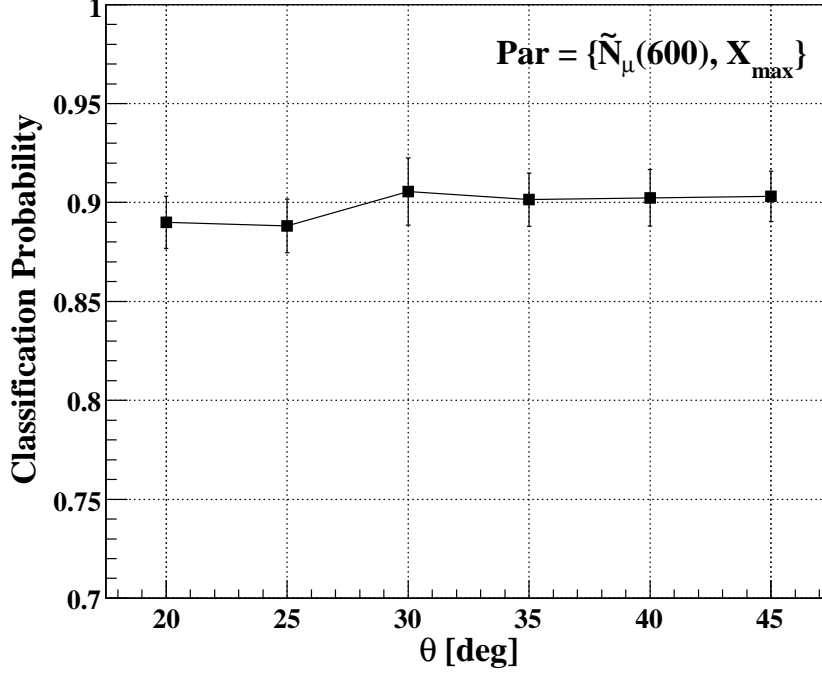


Fig. 9. Classification probability as a function of zenith angle corresponding to $\{\tilde{N}_\mu(600), X_{max}\}$ and hadronic interaction model QGSJET-II. The proton and iron nuclei density estimates of this pair of parameters used for the analysis correspond to QGSJET-II and $\theta = 30^\circ$ (see text for details).

where $\theta_{ref} = 30^\circ$ is a reference angle. In this way a pair of mass sensitive parameters, $\{\tilde{N}_\mu(600), X_{max}\}$, that are almost constant with θ is obtained. Therefore, the estimates corresponding to $\theta = 30^\circ$ can be used to obtain the classification probability as a function of zenith angle for this pair of parameters.

The 20 pairs of proton and iron samples, corresponding to $\theta = 30^\circ$ and QGSJET-II, are used to construct the corresponding density estimates for $\vec{x} = (\tilde{N}_\mu(600), X_{max})$. Then the single pairs of proton and iron samples corresponding to $\theta = 20^\circ, 25^\circ, 35^\circ, 40^\circ, 45^\circ$ (just one pair of proton and iron samples of the 20 available for $\theta = 40^\circ$ is considered) is used to calculate the classification probability as a function of θ , see appendix B for details of the calculation.

Figure 9 shows the obtained classification probability as a function θ . The result corresponding to $\theta = 30^\circ$, obtained in the previous subsection (see table 1), is included in the figure. From this figure it can be seen that the classification probability is almost constant with θ and the mean value is approximately 0.9.

5 Composition of a sample

The determination of the composition of a sample of size $N = N_{pr} + N_{fe}$, where N_{pr} and N_{fe} are the number of protons and iron nuclei, respectively, consists in the estimation of the proton content, i.e., $c_p = N_{pr}/N$. For that purpose suppose that the classification probabilities obtained for a given set of parameters are P_{cl}^{pr} and P_{cl}^{fe} for protons and iron nuclei, respectively. Therefore, the number of proton and iron events correctly classified follow the binomial distribution,

$$P(n_{pr}) = \binom{N_{pr}}{n_{pr}} (P_{cl}^{pr})^{n_{pr}} (1 - P_{cl}^{pr})^{N_{pr} - n_{pr}}, \quad (29)$$

$$P(n_{fe}) = \binom{N_{fe}}{n_{fe}} (P_{cl}^{fe})^{n_{fe}} (1 - P_{cl}^{fe})^{N_{fe} - n_{fe}}. \quad (30)$$

The number of events classified as protons or as iron nuclei are $n_{pr}^{cl} = n_{pr} + N_{fe} - n_{fe}$ and $n_{fe}^{cl} = n_{fe} + N_{pr} - n_{pr}$, respectively. By using Eqs. (29, 30) to calculate the expected values of these quantities the following expressions are obtained,

$$\begin{pmatrix} E[n_{pr}^{cl}] \\ E[n_{fe}^{cl}] \end{pmatrix} = \mathbf{P} \begin{pmatrix} N_{pr} \\ N_{fe} \end{pmatrix} = \begin{pmatrix} P_{cl}^{pr} & 1 - P_{cl}^{fe} \\ 1 - P_{cl}^{pr} & P_{cl}^{fe} \end{pmatrix} \begin{pmatrix} N_{pr} \\ N_{fe} \end{pmatrix}. \quad (31)$$

Last equation suggests the following definition of estimators of N_{pr} and N_{fe} [25],

$$\begin{pmatrix} \hat{N}_{pr} \\ \hat{N}_{fe} \end{pmatrix} = \mathbf{P}^{-1} \begin{pmatrix} n_{pr}^{cl} \\ n_{fe}^{cl} \end{pmatrix}, \quad (32)$$

which, as a function of n_{pr} and n_{fe} give,

$$\hat{N}_{pr} = \frac{N_{fe}P_{cl}^{fe} + N_{pr}(P_{cl}^{fe} - 1) + n_{pr} - n_{fe}}{P_{cl}^{pr} + P_{cl}^{fe} - 1}, \quad (33)$$

$$\hat{N}_{fe} = \frac{N_{pr}P_{cl}^{pr} + N_{fe}(P_{cl}^{pr} - 1) + n_{fe} - n_{pr}}{P_{cl}^{pr} + P_{cl}^{fe} - 1}. \quad (34)$$

Note that, by construction, $E[\hat{N}_{pr}] = N_{pr}$ and $E[\hat{N}_{fe}] = N_{fe}$ (the estimates are non-biased). Therefore, the composition estimator $\hat{c}_p = \hat{N}_{pr}/N$ is also

non-biased and the variance, obtained from Eq. (33) using (29) and (30), is

$$Var[\hat{c}_p] = \frac{1}{N} \frac{P_{cl}^{pr}(1 - P_{cl}^{pr})c_p + P_{cl}^{fe}(1 - P_{fe}^{pr})(1 - c_p)}{(P_{cl}^{pr} + P_{cl}^{fe} - 1)^2}. \quad (35)$$

Note that the variance is inversely proportional to the sample size.

As shown in subsection 4.1, P_{cl}^{pr} and P_{cl}^{fe} are random variable. This happens because finite samples of events are used as test samples as well as to construct the density estimates. Therefore, the distributions of P_{cl}^{pr} and P_{cl}^{fe} , obtained in subsection 4.1, correspond to samples of ~ 2500 events to construct the density estimates as well as for the test samples size.

The lowest values corresponding to the region of 68% of probability of the distributions of P_{cl}^{pr} and P_{cl}^{fe} (see table 1 for $\theta = 30^\circ$ and QGSJET-II) are used to obtain an upper limit of the uncertainty in the determination of the composition of a sample, $\sigma[\hat{c}_p] = Var[\hat{c}_p]^{1/2}$. This approximation overestimates the error because, as mentioned, the classification probability distributions also include the fluctuations due to the finite size of the test samples. In fact, the standard deviation for these fluctuations is $\sigma_{fs} = [p(1 - p)/N]^{1/2}$, where p is the classification probability of protons or iron nuclei corresponding to a given pair of density estimates. $\sigma_{fs} \lesssim 0.01$ for samples of ~ 2500 events and $p = 0.7 - 0.9$. From table 1, it can be seen that such fluctuations are comparable to the total fluctuations. Test samples of much larger size are needed to obtain the classification probability distributions corresponding to density estimates built from samples of ~ 2500 events, without including such fluctuations. Note that also changing the number of events of the samples used to construct the density estimates would modify the fluctuations on the classification probability distributions, in fact, such fluctuations can be reduced by using samples of larger number of events.

Figure 10 shows $\sigma[\hat{c}_p]$ as a function of c_p for the different sets of parameters considered, $\theta = 30^\circ$, QGSJET-II and for samples of 100 events, which is the number of hybrid events expected for the energy interval Π_r in two years of data taking of AMIGA and HEAT [31]. As mentioned, $\sigma[\hat{c}_p]$ is calculated by using the lowest values of the region of 68% of probability corresponding to the proton and iron classification probability distributions. From this figure it can be seen that $\sigma[\hat{c}_p]$ varies very slowly with c_p because the classification probability for protons and iron nuclei are quite similar (see table 1). As expected, the larger the proton and iron classification probabilities the smaller the values of $\sigma[\hat{c}_p]$.

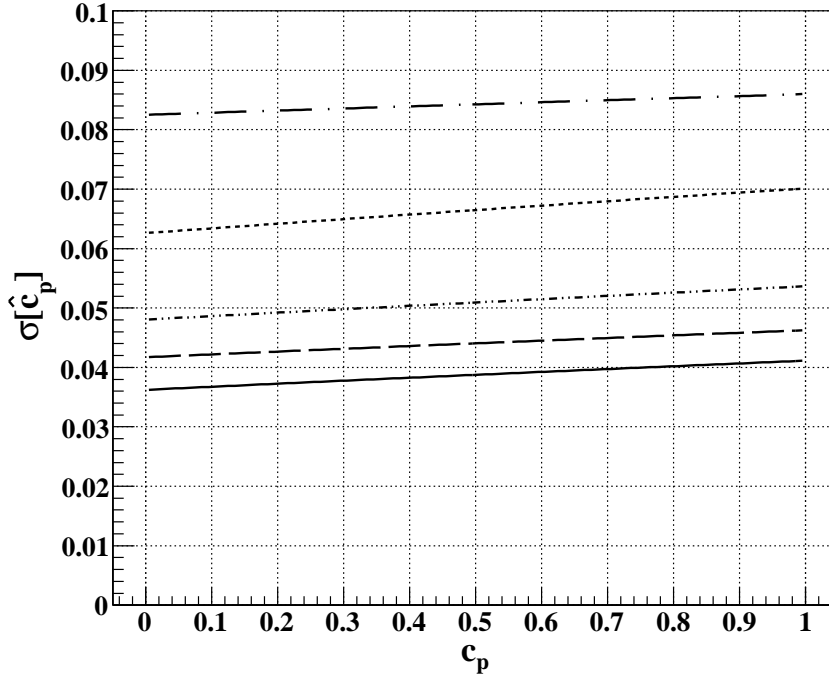


Fig. 10. $\sigma[\hat{c}_p]$ as a function of c_p obtained by using the lowest values of region of 68% of probability corresponding to the proton and iron classification probability distributions, for samples of 100 events, $\theta = 30^\circ$ and hadronic interaction model QGSJET-II. The curves correspond to: from bottom to top, *All* parameters, $\{N_\mu(600), X_{max}\}$, $\{X_{max}, SD\}$, $\{N_\mu(600), SD\}$ and *SD*.

6 Conclusions

Under the assumption of a binary mixture of proton and iron nuclei, we study the possibility of assigning a statistically meaningful classification probability to individual cosmic ray showers in the ankle region of the spectrum. We use a non-parametric technique to estimate the relevant multi-dimensional density functions for the different combinations of parameters that will be available from the Auger enhancements AMIGA and HEAT.

We find that, as expected, the maximum classification probability is obtained by combining simultaneously all surface and fluorescence parameters ($\sim 92\%$ for QGSJET-II). However, the two leading parameters are $\{N_\mu(600), X_{max}\}$ which, used in a two-dimensional analysis, already give a classification probability almost as large as the whole set of parameters combined ($\sim 91\%$ for QGSJET-II). This means that, the separation between protons and iron nuclei, is mainly expressed experimentally through these two parameters.

We also study the effect of assuming QGSJET-II as the true hadronic interaction model (used to construct the density estimates) when the real one

is Sibyll 2.1 (used to obtain the test samples) and vice versa. We find that the classification probabilities obtained in either case, have systematic differences which are much smaller than their statistical fluctuations. This happens because the hadronic interaction models considered produce similar air showers and, consequently, similar mass sensitive parameters. Nevertheless, other models, like EPOS [47], which predict a very different shower muon content, would affect the composition estimates obtained with our technique. If the later were the case, a possible way out might come from the application of a bi-dimensional technique, in which X_{max} and N_μ information from hybrid events is used simultaneously in order to disentangle the hadronic uncertainty from the composition effects (see Ref. [34]).

Although the values of the classification probability, obtained for the different sets of parameters considered, do not allow a reliable classification into proton and iron primaries on an event-by-event bases, the composition of a sample can be estimated with reasonable accuracy using this technique. It must be kept in mind, however, that any composition estimate inside this framework, is bounded by the simplifying assumptions of a binary mixture and of a hadronic interaction model that is well represented by either QGSJET-II or Sibyll 2.1. The limitation to a mixture of two components is not actually a limitation of our mathematical formulation, as expressed for example in Section 2, but a realization of the limitations posed by intrinsic shower fluctuations, detector uncertainties and limitations and the lack of a precise knowledge of the hadronic interactions. Regarding the latter, the most widely used models in the literature are at present QGSJET and Sibyll in their latest versions, which we use in the present work. Even if the differences between these two models are not large enough as to render our results ambiguous, these models could be wrong. In fact, as already mentioned, the new model EPOS predicts a much higher number of muons for a given nuclei at any energy. Needless to say, these constraints apply not only to our own, but to any technique that attempts to determine composition, and they are important factors to which accelerator particle physics will certainly make a fundamental contribution in the near future.

7 Acknowledgments

The authors have greatly benefited from discussions with several colleagues from the Pierre Auger Collaboration, of which they are members. GMT acknowledges the support of DGAPA-UNAM through grant IN115707.

A Effect of the non independence of the events

The computer processing time and disk space required to obtain several samples of showers with good statistics are very large. Therefore, each simulated shower is used 50 times, to increase the statistics, by uniformly distributing impact points in the array area (see section 3). The simulated events generated in this way, corresponding to a given sample, are not independent.

A pair of proton and iron samples of 1000 independent events each (showers after detectors simulations) are obtained by taking at random 50 independent events corresponding to 50 independent showers of each of the 20 proton and 20 iron samples available for each zenith angle (30° and 40°) and hadronic interaction model considered. Then, the leave-one-out technique [26] is used to estimate the classification probabilities for each pair of proton and iron samples and combination of parameters considered.

Table A.1 shows the classification probabilities obtained for $\theta = 30^\circ$ and QGSJET-II for the different combination of parameters considered. Although the number of events corresponding to the proton and iron samples composed by independent events is ~ 2.4 times smaller than the one used for the analysis of subsection 4.1, the obtained values of the classification probabilities P_{cl}^{pr} , P_{cl}^{fe} and P_{cl} of table A.1 are contained in the region of 68% of probability of the corresponding distributions for the non-independent event samples (see table 1).

Table A.1

Classification probability corresponding to protons, iron nuclei and both together, obtained from two samples, one for protons and the other for iron, of 1000 independent events each, for $\theta = 30^\circ$ and high energy hadronic interaction model QGSJET-II.

Parameters	P_{cl}^{pr}	P_{cl}^{fe}	P_{cl}
<i>All</i>	0.88	0.92	0.90
$N_\mu + X_{max}$	0.88	0.91	0.89
$X_{max} + SD$	0.84	0.88	0.86
$N_\mu + SD$	0.83	0.84	0.83
<i>SD</i>	0.74	0.79	0.77

Similar results were obtained for $\theta = 40^\circ$ and for Sibyll 2.1 as well as for the cases in which one hadronic interaction model is used to construct the density estimates and the other for the test samples. For all these cases the results obtained for the samples composed by independent events are compatible with the corresponding to the samples composed by non-independent events.

B Calculation of the classification probability using a single test sample

In this appendix details of the calculation of the classification probability and their uncertainties corresponding to the pair of parameters $\{\tilde{N}_\mu(600), X_{max}\}$ (see subsection 4.2) are given.

The pair of proton and iron samples of number of events N_{pr} and N_{fe} , respectively, for a given zenith angle is used together with 20 pairs of proton and iron density estimates corresponding to $\theta = 30^\circ$. In this way, 20 different values for protons and 20 for iron nuclei of the number of events correctly classified are obtained (see Eqs. (25, 26, 27)): $n_{pr}^0(s)$ and $n_{fe}^0(s)$ with $s = 1, \dots, M$ and $M = 20$.

The distribution function of the number of events correctly classified is binomial, therefore, including the uncertainty in the determination of the parameter p of the binomial distribution, inferred from a given number of positive trials $n_A^0(s)$, the following expression is obtained,

$$P(n_A|N_A, n_A^0(s)) = \binom{N_A}{n_A} \int_0^1 dp p^{n_A} (1-p)^{N_A-n_A} B(p|n_A^0(s)+1, N_A+n_A^0(s)-1), \quad (\text{B.1})$$

where,

$$B(p|\alpha, \beta) = \frac{\Gamma(\alpha + \beta)}{\Gamma(\alpha) \Gamma(\beta)} p^{\alpha-1} (1-p)^{\beta-1}, \quad (\text{B.2})$$

is the Beta distribution and $\Gamma(x)$ is the Gamma function.

The distribution function of n_A can be estimated from,

$$f(n_A) = \frac{1}{M} \sum_{s=1}^M P(n_A|N_A, n_A^0(s)). \quad (\text{B.3})$$

Therefore, the mean value and standard deviation of the classification probability, $P_{cl}^A = n_A/N_A$, are given by,

$$E[P_{cl}^A] = \frac{1}{MN_A} \sum_{s=1}^M E[n_A(s)], \quad (\text{B.4})$$

$$\sigma[P_{cl}^A] = \frac{1}{N_A} \left[\frac{1}{M} \sum_{s=1}^M (\sigma[n_A(s)]^2 + E[n_A(s)]^2) - E[P_{cl}^A]^2 \right]^{1/2}, \quad (\text{B.5})$$

by using Eq. (B.1) they become,

$$E[n_A(s)] = N_A \frac{n_A^0(s) + 1}{N_A + 1}, \quad (\text{B.6})$$

$$\sigma[n_A(s)]^2 = E[n_A(s)](1 - E[n_A(s)]) + \frac{(N_A - 1)(N_A - n_A^0(s) + 1)(n_A^0(s) + 1)}{(N_A + 2)^2(N_A + 3)}. \quad (\text{B.7})$$

Finally, the mean value and the standard deviation of P_{cl} are estimated from,

$$E[P_{cl}] = \frac{1}{MN} \sum_{s=1}^M E[n(s)], \quad (\text{B.8})$$

$$\sigma[P_{cl}] = \frac{1}{N} \left[\frac{1}{M} \sum_{s=1}^M (\sigma[n(s)]^2 + E[n(s)]^2) - E[P_{cl}]^2 \right]^{1/2}, \quad (\text{B.9})$$

where $N = N_{pr} + N_{fe}$, $E[n(s)] = E[n_{pr}(s)] + E[n_{fe}(s)]$ and $\sigma[n(s)]^2 = \sigma[n_{pr}(s)]^2 + \sigma[n_{fe}(s)]^2$.

References

- [1] K. H. Kampert et al., KASCADE Collaboration, arXiv:astro-ph/0405608.
- [2] M. Aglietta et al., EAS-TOP and MACRO Collaboration, *Astropart. Phys.* **20**, 641 (2004).
- [3] T. Antoni et al., *Astropart. Phys.* **24**, 1 (2005).
- [4] M. Nagano et al., *J. Phys. G* **10**, 1295 (1984).
- [5] T. Abu-Zayyad et al., *Astrophys. J.* **557**, 686 (2001).
- [6] M. I. Pravdin et al., *Proc. 28th ICRC (Tuskuba)* 389 (2003).
- [7] R.U. Abbasi et al., HiRes Collaboration, *Phys. Rev. Lett.* **92**, 151101 (2004).
- [8] Y. Tokonatsu for the Pierre Auger Collaboration, *Proc. 30th ICRC (Mérida-México)*, #318 (2007).
- [9] D. Bergman for the HiRes Collaboration, *Proc. 30th ICRC (Mérida-México)*, #1128 (2007).
- [10] K. Greisen, *Phys. Rev. Lett.* **16**, 748 (1966).
- [11] G. Zatsepin y V. Kuz'min, *Zh. Eksp. Teor. Fiz. Pis'ma Red.* **4**, 144 (1966).
- [12] D. Allard, E. Parizot, E. Khan, S. Goriely and A. V. Olinto, *Astron. Astrophys.* **443**, L29 (2005).

- [13] J.R. Hoerandel, *Astropart. Phys.* **19**, 193 (2003).
- [14] J. Candia et al., *JHEP* **0212**, 033 (2002).
- [15] V. Berezhinsky, S. Grigor'eva and B. Hnatyk, *Astropart. Phys.* **21**, 617 (2004).
- [16] M. Ave et al., *Proc. 27th ICRC (Hamburg)* 381 (2001).
- [17] M. Takeda et al., *Astropart. Phys.* **19**, 447 (2003).
- [18] D. Allard, E. Parizot and A. V. Olinto, *Astropart. Phys.* **27**, 61 (2007).
- [19] T. Wibig and A. Wolfendale, *J. Phys.* **G31**, 255 (2005).
- [20] G. Medina-Tanco for the Pierre Auger Collaboration, *Proc. 30th ICRC (Mérida-México)*, #991 (2007).
- [21] G. Medina-Tanco, *Proceedings of the Mexican School on Astrophysics 2005 (EMA 2005)*, arXiv:astro-ph/0607543.
- [22] C. De Donato and G. Medina-Tanco, *Proc. 30th ICRC (Mérida-México)*, #1249 (2007).
- [23] M. T. Dova, A. Mariazzi and A. Watson, *Proc. 29th ICRC* **7**, 275 (2005).
- [24] R. Engel for the Pierre Auger Collaboration, *Proc. 30th ICRC (Mérida-México)*, #605 (2007).
- [25] T. Antoni et. al., *Astropart. Phys.* **16**, 245 (2002).
- [26] A. A. Chilingarian, *Comput. Phys. Commun.* **35**, 441 (1989).
- [27] M. A. K. Glasmacher et. al., *Astropart. Phys.* **12**, 1 (1999).
- [28] A. Tiba, G. Medina-Tanco and S. Sciutto, arXiv:astro-ph/0502255.
- [29] A. Etchegoyen for the Pierre Auger Collaboration, *Proc. 30th ICRC (Mérida-México)*, #1307 (2007).
- [30] H. Klages for the Pierre Auger Collaboration, *Proc. 30th ICRC (Mérida-México)*, #65 (2007).
- [31] M. C. Medina et al., *Nucl. Inst. and Meth.* **A566**, 302 (2006).
- [32] T. Bayes, *Pil. Trans. Roy. Soc.* **53**, 54 (1763) (reprinted in *Biometrika* **45**, 296 (1958)).
- [33] M. Roth for the Pierre Auger Collaboration, *Proc. 30th ICRC (Mérida)*, #313 (2007).
- [34] A. D. Supanitsky, G. Medina-Tanco and A. Etchegoyen, submitted to a refereed magazine.
- [35] S. Sciutto, *AIRES user's Manual and Reference Guide* (2002), <http://www.fisica.unlp.edu.ar/auger/aires>.

- [36] S. Ostapchenko, arXiv:astro-ph/0412591 (2004).
- [37] S. Ostapchenko, arXiv:hep-ph/0501093 (2005).
- [38] R. Engel, T. Gaiser, P. Lipari y T. Stanev, Proc. 26th ICRC **1**, 415 (2000).
- [39] A. D. Supanitsky et. al., Astropart. Phys. **29**, 461 (2008).
- [40] <http://www.auger.org.ar/CDAS-Public>.
- [41] B. Silvermann, *Density Estimation for Statistics and Data Analysis*, ed. Chapman & Hall, New York (1986).
- [42] D. Scott, *Multivariate Density Estimation*, ed. Wiley, New York (1992).
- [43] D. Fadda, E. Slezak y A. Bijaoui, Astron. Astrophys. Suppl. Ser. **127**, 335 (1998).
- [44] D. Marritt y B. Tremblay, Astron. J. **108**, 514 (1994).
- [45] A. D. Supanitsky and G. Medina-Tanco, to be published in Astropart. Phys. (arXiv:0810.2251).
- [46] P. Ghia for the Pierre Auger Collaboration, Proc. 30th ICRC (Mérida), #300 (2007).
- [47] K. Werner et al., Phys. Rev. **C74**, 044902 (2006).